ARTICLE

Core−Shell Hybrid Nanoparticles with Functionalized Quantum Dots and Ionic Dyes: Growth, Monolayer Formation, and Electrical Bistability

Bikas C. Das and Amlan J. Pal*

Indian Association for the Cultivation of Science, Department of Solid State Physics and Centre for Advanced Materials, Jadavpur, Kolkata 700032, India

ABSTRACT We report growth, monolayer formation, and (electrical bistability and memory phenomenon) properties of hybrid core−shell nanoparticles. While inorganic quantum dots, such as CdS or CdSe, act as the core, a monolayer of ionic organic dye molecules, electrostatically bound to the surface of functionalized quantum dots, forms the shell. We form a monolayer of the core−shell hybrid nanoparticles *via* a layer-by-layer electrostatic assembly process. Growth and monolayer formation of the organic−inorganic hybrid nanoparticles have been substantiated by usual characterization methods, including electronic absorption spectroscopy of dispersed solution and atomic force microscope images of scratched films. Devices based on the hybrid nanoparticles have exhibited electrical bistability and memory phenomena. From the comparison of these properties in core−shell nanoparticles and in its components, we infer that the degree of conductance switching or on/off ratio is substantially higher in the hybrid nanoparticles. Also, they (core−shell particles) provide routes to tune the bistability and memory phenomena by choosing either of the components. A monolayer of hybrid nanoparticles has been characterized by a scanning tunneling microscope tip as the other electrode. We show that a single core−shell hybrid nanoparticle can exhibit bistability with an associated memory phenomenon. Charge confinement, as evidenced by an increase in the density of states, has been found to be the mechanism of electrical bistability.

KEYWORDS: organic−inorganic hybrid nanoparticles · core−shell nanoparticles · monolayer formation · electrical bistability · scanning tunneling microscopy · charge confinement · bistable nanodevices

*Address correspondence to sspajp@iacs.res.in.

Received for review June 2, 2008 and accepted July 29, 2008.

Published online August 5, 2008.
10.1021/nn800335f CCC: $40.75

Growth and functionalities of semiconducting nanoparticles are being studied in great detail due to their interest ranging from fundamental chemistry to application possibilities. Functionalization of nanoparticles has become important to suffice both the basic requirements (such as solubility)[1−7] and their application outlooks.[8−11] Different core−shell nanoparticles, such as ones with two different inorganic semiconductors,[6,12−15] small organic molecules, or amphiphilic polymers attached to inorganic nanocrystals through ligand exchange protocols,[16] or quantum dots coated with biological molecules,[17−19] have been synthesized and characterized. In such cases, processibility or solubility of core−shell nanoparticles is generally achieved with the use of amphiphilic polymers consisting of hydrophilic side chains such as $-COO^-$; hydrophobic headgroups of the amphiphile provide the linkage to the nanoparticles. The hydrophilic part also provides sites for further functionality on the surface of semiconducting nanoparticles.

In this article, we show that core−shell organic−inorganic hybrid nanoparticles can also be grown *via* electrostatic interaction between a functionalized inorganic core and ionic organic-dye molecules. Such a combination will allow tuning of functionalities of core−shell nanoparticles by controlling parameters of one of the components. Addressing a single (core−shell) nanoparticle will enhance the density of any function to a higher level. Hence, a monolayer or a two-dimensional array of hybrid nanoparticles, formed following layer-by-layer (LbL) electrostatic assembly route,[4−6,20−22] can be of immense importance.

In recent years, inorganic quantum dots and some organic molecules have shown applications as memory elements.[23−31] In such materials, electrical bistability, which is manifested as current−voltage characteristics being dependent on the preceding voltage pulses or voltage-sweep directions, leads to memory applications. In semiconducting nanoparticles, electrical bistability arises due to charge confinement.[23−28] Conformation change and/or electroreduction of organic molecules plays a key role in changing the conductivity of the molecules.[29,32−34] It will hence be intriguing to study bistability in inorganic−organic hybrid core−shell nanoparticles and compare it with that in its components. In this article, we report

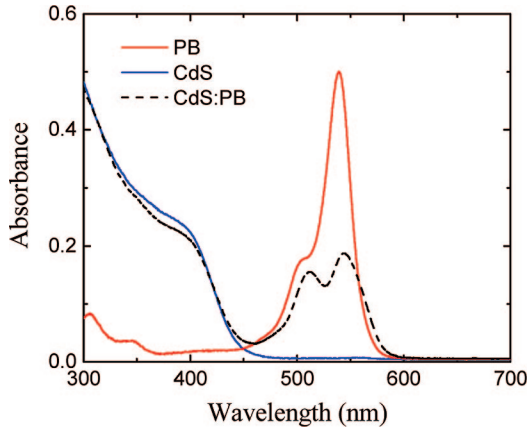

Figure 1. Electronic absorption spectra of Phloxine B (PB) solution (5 μM), CdS nanoparticles, and PB-coated CdS nanoparticles (CdS:PB) in dispersed solution (15 μg/mL).

growth, formation of a monolayer, and characterization of hybrid core−shell nanoparticles consisting of inorganic quantum dots in the core and a monolayer of organic dye molecules as the shell for electrical bistability and memory applications. We choose dye molecules in the xanthene class that undergo conformational change during conductance switching.

RESULTS AND DISCUSSION

Growth of Core−Shell Hybrid Nanoparticles. To confirm adsorption of organic dyes on inorganic nanoparticles, we have recorded electronic absorption spectra of the hybrid nanoparticles and their components (Figure 1). The spectra for the nanoparticles and Phloxine B (PB) dye show bands at the usual wavelengths. Diameter of the nanoparticles, as calculated from the peak wavelength (390 nm), effective mass of electron, and band gap of the bulk CdS (=2.42 eV), has turned out to be 5.5 nm, which has remained invariant due to dye absorption. Formation of core−shell nanoparticles with other dye molecules in the xanthene class or on CdSe nanoparticles was similarly established by recording electronic absorption spectra. Figure S1 in the Supporting Information displays absorption spectra of CdSe:PB, CdSe:Rose Bengal (RB), CdSe:erythrosin B (EB), CdSe:eosin Y (EY), and CdSe:fluorescein sodium (FS) core−shell nanoparticles.

Relative intensities of the two bands of PB, however, differed in solution and when the molecules were anchored on the nanoparticles. Lowering of the intensity of the 0−0 band in the spectrum of PB solution could be due to formation of PB aggregates. This is supported by the observation that, with a decrease in PB concentration in solution, the ratio of the intensities of the bands at 507 and 543 nm (I_{507}/I_{543}) increases. Electronic absorption spectra of PB at different concentrations and a plot of the ratio of the two bands *versus* PB concentration are shown in Figure S2 in the Supporting Information. With an increase in PB concentration in the solution, a decrease in relative intensity of the 0−0 band (at 507 nm) is due to PB aggregates. Since the ratio of the two bands of PB in CdS:PB core−shell matches the ratio obtained in the absorption spectrum of PB in its lowest concentration, we infer that the dye molecules adsorbed on CdS nanoparticles did not form aggregates.

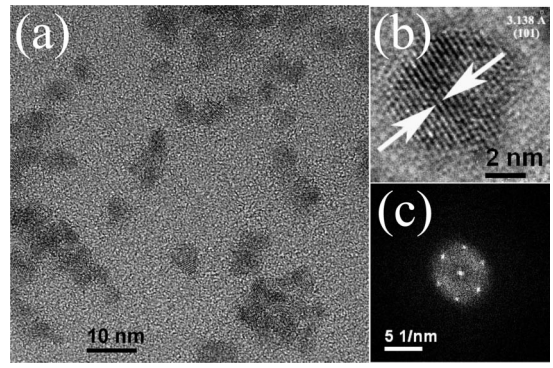

Figure 2. (a) TEM image of CdS:phloxine B hybrid core−shell nanoparticles, (b) HR-TEM image of a single hybrid nanoparticle and (c) corresponding FFT pattern of a single nanoparticle.

Growth of the nanoparticles has been supported by X-ray diffraction (XRD) spectra, energy dispersive X-ray (EDX) analyses, selected-area electron diffraction (SAED) patterns, and transmission electron microscopy (TEM) and high-resolution TEM (HR-TEM) images. Adsorption of organic molecules on nanoparticles has been substantiated by Fourier transform infrared (FT-IR) spectra and the UV−visible spectra of the LbL films of core−shell nanoparticles deposited with a polyanion (as discussed later). While the EDX analyses evidence composition of the nanoparticles (Figure S3 in the Supporting Information), the XRD spectra and SAED patterns show the crystal planes of CdS (Figure S4 and S5, respectively, in the Supporting Information). To monitor the composition of the core of core−shell nanoparticles before and after PB coating, we recorded EDX analysis and SAED patterns. Part b of Figure S3 and Figure S5 show that there was little or no change in the composition or crystal planes of CdS nanoparticles due to PB adsorption. A typical TEM image of CdS nanoparticles (Figure 2a) shows isolated particles over the fields of view, ruling out formation of aggregates. HR-TEM images of the nanoparticles, as presented in Figure 2b, and its corresponding FFT pattern (Figure 2c) show lattice spacing of CdS crystals (0.314 and 0.309 nm, respectively). The values match very well with the lattice spacing for the (101) plane of CdS crystals, as mentioned at JCPDS PDF No. 41-1049. Size of the nanoparticles, as estimated from HR-TEM images over a larger area, has been projected to be about 5.6 nm. Infrared absorption spectrum of PB-coated nanoparticles shows bands at 1240, 1449, 1546, 1610, and 3400 cm^{-1} corresponding to stretching vibration of acidic C−O, aromatic C═C, primary amine N−H bending vibration, acidic C═O, and primary amine N−H stretching vibration

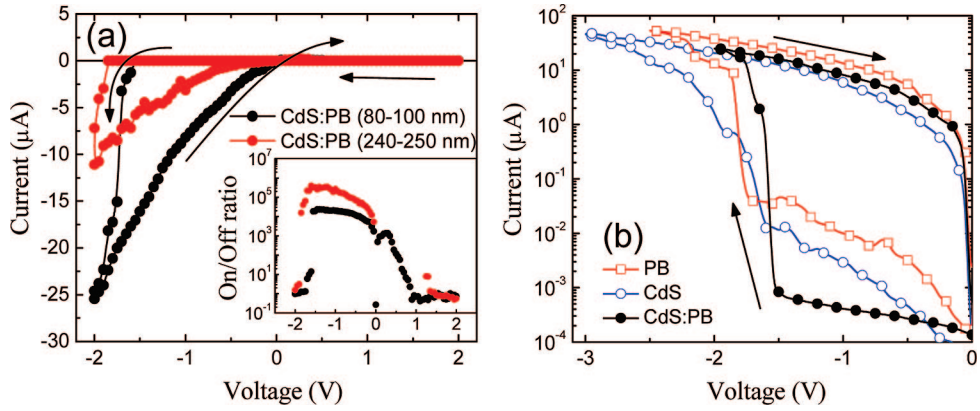

Figure 3. (a) Current−voltage characteristics of devices based on phloxine B (PB)-coated CdS nanoparticles in a PMMA matrix under a voltage loop. Thicknesses of the active layer are mentioned in the legends. (b) Reverse bias section of the characteristics of devices based on PB molecules, CdS nanoparticles, and PB-coated CdS nanoparticles are shown for comparison. Here, thickness of the active layer was 80−100 nm. Arrows show the direction of voltage sweep. The inset of (a) shows plots of on/off ratio *versus* voltage for the devices based on core−shell nanoparticles.

modes, respectively (Figure S6 in the Supporting Information). Appearance of the vibrational modes of the organic material supports adsorption of the dye molecules on the nanoparticles. Electrostatic adsorption of dye molecules on the surface of functionalized nanoparticles itself assures that only a molecular layer of the organic material forms on CdS nanoparticles. Due to the cationic nature of the surface of the nanoparticles (the nanoparticles was stabilized with cysteamine hydrochloride, CAH) and anionic nature of the organic dye molecules, multilayer of the dyes would not be possible. In a subsequent section (Monolayer Formation), we will show that surface coating of the nanoparticles with the dye molecules was not total; that is, some CAH of the nanoparticles was still exposed for further electrostatic binding.

Current−Voltage Characteristics of Hybrid Nanoparticles in a Polymer Matrix. Since the nanoparticles and organic dye molecules exhibit electrical bistability, it is intriguing to study conductance switching in the hybrid systems and compare the results with that in its components. Current−voltage (*I*−*V*) characteristics of devices based on CdS:PB hybrid nanoparticles in a poly(methyl methacrylate) (PMMA) matrix under a voltage loop are shown in Figure 3a. Results for two different thicknesses of the active layer are presented in the figure. In Figure 3b, the results in the core−shell nanoparticles have been compared with those in devices based on the components (*i.e.*, CdS nanoparticles and PB molecules (both in PMMA matrix) for a particular thickness). The plots show that, during a sweep toward the negative voltage, a transition in current from a low value to a high one occurs. In other words, the materials switch to a high conducting state. In organic dyes, the switching is generally due to a change in the molecules' conformation or electroreduction. In semiconducting nanoparticles, on the other hand, the bistability has so far been discussed in terms of charge confinement in the nanoparticles. A comparison of the *I*−*V* characteristics of the hybrid nanoparticles and their components shows that the magnitude of voltage at which the device switches is lower in the hybrid system. This indicates that the bistability in hybrid core−shell nanoparticles is more easily achievable than in its components. Moreover, the on/off ratio, the ratio between the current values of the two conducting states, at any voltage is higher in the device based on (hybrid) core−shell nanoparticles. For the core−shell nanoparticle based device, the ratio reaches up to 2×10^4, which is at least an order of magnitude higher than that in devices based on the components of the same thickness. Higher ratio in the core−shell case may be due to simultaneous occurrence of charge confinement in the nanoparticles and conformational change of organic dye molecules. The on/off ratio *versus* voltage plots for the core−shell cases are shown in the inset of Figure 3a. Since both the parameters are advantageous for memory applications, the hybrid organic−inorganic system provides a newer route to design memory elements.

While the bistability has depended on the choice of material in the core or the dye in the shell, it did not respond to the magnitude of the voltage up to which bias was scanned (V_{max}). Figure S7a in the Supporting Information shows that conductance switching occurs always at around −1.6 V. The bistability in the 0 to −2.0 V range is invariant with the value of $-V_{max}$, showing reproducibility of conductance switching in these systems. Reproducible bistability for memory applications can best be understood from the *I*−*V* plots under a voltage loop. Figure S7b in the Supporting Information shows that, when voltage is scanned in multiple loops, current values with all the features of electrical bistability (that is, switching on to a high state and off to a low conducting state) are reproduced in all the loops. In other words, current at a voltage always depends on the direction of sweep or the preceding voltage pulse. This exemplifies possibilities of memory phenomena in these core−shell hybrid nanoparticles (as discussed in the next section).

Before evidencing memory phenomena, it is worthwhile to discuss the possible mechanisms of electrical bistability in semiconducting nanoparticles and organic dye molecules. Mechanism of conductance switching in organic dyes is still being discussed; depending on

the functionalities of the molecule and electrode combination used, the mechanism can be (i) conformational change of the molecules,[29,32] (ii) electroreduction to a high conducting state,[33] or (iii) formation of metal filaments.[35] In the nanoparticles, it has so far been explained in terms of charge confinement, leading to an increase in the density of states.[23−28] We have tried to fit the *I*−*V* characteristics of the devices based on core−shell nanoparticles with the existing models. First of all, with dissimilar metal electrodes, the characteristics were expectedly rectifying in nature (Figure S8 in the Supporting Information). Results shown in the Figure S9a and 9b in the Supporting Information show moderate fit to ln(*I*) *versus* $V^{1/2}$ plot for low conducting state and ln(*G*) *versus* $E^{-1/2}$ plot for the high state, respectively, for devices with both the thicknesses. Here *G* and *E* represent conductance and electric field of/across the devices, respectively. For the low conducting states, the current is hence injection-limited; the mechanism changes to a bulk-dominated one (variable range hopping at high field[36]) in the high conducting state. That is, with conductance switching, there has been a change in the mechanism of conduction in the devices. Cole−Cole plots (a plot of real *versus* imaginary parts of complex impedance with test frequency as an independent variable) of devices based on core−shell nanoparticles in their low and high conducting states are semicircular in nature with a 25 Ω shift from the origin. While the small resistance is due to the contacts, the semicircular plot shows a decrease in the diameter upon conductance switching (Figure S10 of the Supporting Information). Here we have recorded complex impedance under 0 V dc bias in the 1−12 MHz region after application of a positive or a negative voltage pulse, which induce the low and high conducting states, respectively. Since the diameter of such plots represents bulk resistance of the device,[37] the results show that, upon application of a negative voltage pulse, the bulk resistance of the thin film must have changed due to presumably charge confinement in the hybrid core−shell nanoparticles.

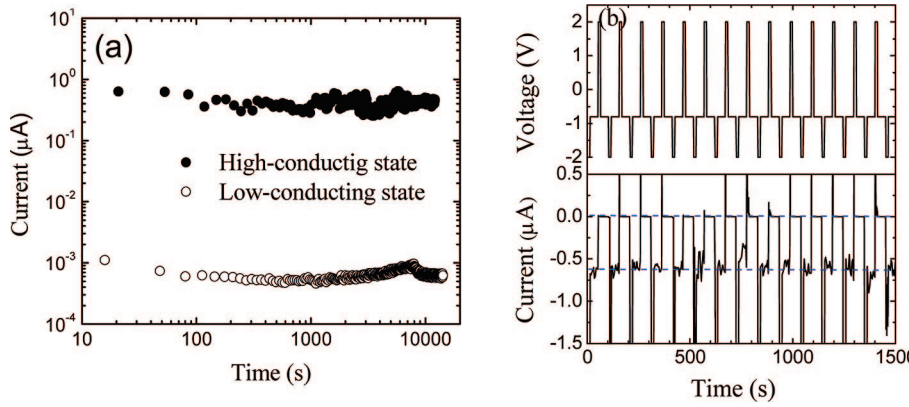

Figure 4. (a) Read-only memory and (b) random-access memory applications of a device based on CdS:PB hybrid nanoparticles in a PMMA matrix. In (a), the high and the low states were induced by applying −2.0 and +2.0 V pulse (width = 10 s), respectively. Magnitude of current under −0.8 V pulse (width = 2 s; duty cycle = 6.25%) as a function of time is plotted in the figure. Voltage sequence and its corresponding current are presented in the two panels of (b). Broken lines in the lower panel represent the levels of current under the probe voltage for the two conducting states.

Memory Phenomena of Hybrid Nanoparticles in a Polymer Matrix. Reproducible electrical bistability under multiple voltage loops has led us to examine the devices for possible memory applications. Since current at a voltage depends on the direction of voltage sweep, a positive or a negative voltage pulse also would induce different conducting states. If we can "read" the two states by measuring current under a small probe voltage, we will be able to exemplify read-only memory (ROM). Figure 4a shows a plot of device current at −0.8 V as a function of time after a high or a low state is induced. Magnitude of current remained clearly different for the two conducting states, substantiating ROM applications. The ratio between the currents under probe voltage is around 10^3. The two states can also be flip-flopped; that is, we could induce or "write" the two states in sequence and "read" them every time. In Figure 4b, we show a voltage sequence and the corresponding current in a CdS:PB-based device. While probing the high and the low states, the current values remained clearly separable, evidencing RAM applications of the core−shell hybrid nanoparticles.

Monolayer Formation of Hybrid Nanoparticles. It is imperative to bring out the advantages of the size of nanoparticles by scaling down the size of memory elements. In order to do so, we first scaled down the thickness of the device down to a single layer. We aimed to form a monolayer or a two-dimensional array of the core−shell nanoparticles *via* an electrostatic adsorption process. To facilitate the adsorption process, it was crucial to first understand the ionic nature of the core−shell nanoparticles. The CdS core was CAH-capped; that is, in dispersed water, it was cationic in nature. The dye on the shell, on the other hand, was anionic with its $-O^-$ and $-COO^-$ groups. Since we added a low concentration solution of the dye molecule in CdS-dispersed solution, it is unlikely that all the amine groups of CAH will anchor a dye molecule. Irrespective of whether both or one of the $-O^-$ and $-COO^-$ groups of a dye molecule become bound to the surface of a CdS nanoparticle, the CdS:PB core−shell nanoparticles will behave as a cationic one due to the excess $-NH_3^+$ groups of the CAH stabilizer that did not bind any dye molecule. If, on the other hand, most of the $-NH_3^+$ groups of the CAH stabilizer bind one of the $-O^-$ and $-COO^-$ groups of a dye molecule leaving the other aside, the core−shell nanoparticle will act as an anionic one. To find out the

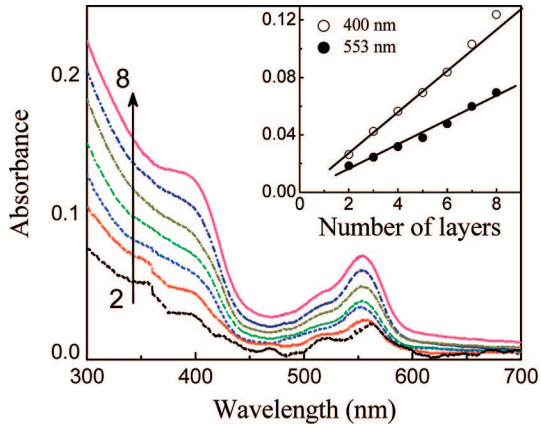

Figure 5. Electronic absorption spectra of (PAA/CdS:PB)$_n$ layers deposited *via* LbL assembly. The arrow represents the direction of increase in absorbance for the 2 to 8 layers of the LbL film. Inset represents absorbance at 400 and 553 nm as a function of number of LbL layers deposited on a quartz substrate.

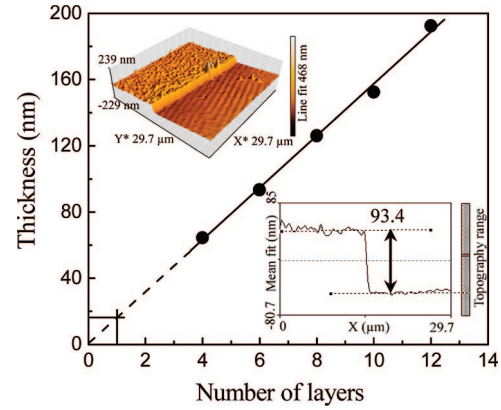

Figure 6. Plot of film thickness of (PAA/CdS:PB)$_n$ deposited *via* LbL electrostatic assembly method *versus* number of layers (*n*). The line, which has been extended to estimate the thickness of one layer, is the best fit to the points. Insets show three-dimensional AFM topography of a scratch on (PAA/CdS:PB)$_6$ film and the obtained depth profile of the scratch.

degree of dye adsorption that has occurred in the present system, we tried to deposit multilayer films of the core−shell nanoaprticles *via* LbL electrostatic assembly method both with a polycation and a polyanion. Depending on the nature of surface charge of CdS:PB hybrid nanoparticles, film deposition will be successful in one of the cases.

We have observed that, while depositing the LbL film with a polyanion (namely, polyacrilic acid, PAA), band intensities of electronic absorption spectra of the dye and nanoparticle, recorded after deposition of every layer of LbL films, increase with the number of PAA/(CdS:PB) layers (Figure 5). Plots of the absorbance at the peak intensities of the dye and the nanoparticle *versus* number of PAA/(CdS:PB) layers are also linear through the origin (inset of Figure 5), showing that the deposition of the core−shell nanoparticles was uniform during the LbL film deposition process. This, moreover, shows that the dye-coated CdS nanoparticles behaved as cationic in nature. Also, the observation that the band intensities corresponding to the dye molecule increase with the number of PAA/(CdS:PB) layers points to the following inference: dye molecules were adsorbed on the surface of the nanoparticles. Had the dye molecules remained isolated or separated in the dispersed solution containing the CAH-coated CdS nanoparticles, the anionic dye molecules would not have become adsorbed on a polyanion layer during the LbL film deposition process. The results hence add a lot of credence to the formation of core−shell hybrid nanoparticles.

As such, LbL deposition method itself assures that only a single layer is deposited during each dipping because further layers will be repelled, forbidding formation of multilayers. We next will show that isolated core−shell nanopartcles and *not* their aggregates were adsorbed during deposition of each layer. To establish this, we have first deposited different bilayers of PAA/(CdS:PB) LbL films; we have scratched each of the films and recorded atomic force microscope (AFM) images at the scratched region to estimate the thickness of each of the films from its depth profile. Since one or two bilayer films are expected to have a too low thickness, we relied on the measurements carried out on films of 4 or more bilayers. Thickness *versus* number of PAA/(CdS:PB) layers are shown in Figure 6. AFM topography and depth profile of one of the scratched films with a constant tip force of 20 nN are also shown in the insets. The figure shows that the thickness of the film increases linearly with the number of deposited LbL layers. The linear fit of the plot approaches the origin. From the extrapolated part of the figure, we have estimated the thickness for a single PAA/(CdS:PB) bilayer. It has returned a value of 16.5 nm, which can be considered as the sum of the thicknesses of a PAA layer and the diameter of hybrid core−shell nanoparticles. The value is quite reasonable considering the diameter of core CdS nanoparticles obtained from the HR-TEM image (5.6 nm).

Electrical Bistability of a Monolayer of Hybrid Nanoparticles. We have characterized the monolayer of hybrid nanoparticles with a scanning tunneling microscope (STM) tip. The monolayer was formed on doped Si wafer, which acted as the base electrode. A two-dimensional STM topography of a monolayer of hybrid nanoparticles is shown in the inset of Figure 7a. The topography shows the presence of nanoparticles on Si substrates (a topography of Si wafer without any layer of nanoparticles has returned a clear image). We have first probed the process of STM imaging and its impact on the monolayer. This was achieved by recording STM topography of a certain area in sequence. Figure S11 in the Supporting Information shows that the finer details of the image of a monolayer of CdS:PB hybrid nanoparticles are reproducibly observed during successive imaging. That is, the STM tip did not peel off the monolayer of core−shell nanoparticles during the imaging pro-

cess. The stability must be due to electrostatic binding of the hybrid nanoparticles with the Si substrates.

I−*V* characteristics of a monolayer of CdS:PB hybrid core−shell nanoparticles, measured with a Pt/Ir tip of a STM under two sweep voltage directions, are shown in Figure 7a. The results show that a single core−shell nanoparticle or a parallel combination of the particles (two-dimensional array) exhibits electrical bistability. The nanoparticles switch to a high state at a suitable positive voltage. The threshold voltage of switching (V_{Th}) is little above +2.0 V. When a negative voltage is applied, the nanoparticles switch back to their original low conducting state. The on/off ratio of the monolayer is higher than 1000. Such a bistability is reproducible over many cycles. A variation in the maximum sweep voltage (V_{max}) has yielded the same V_{Th} and identical electrical bistability (Figure S12a in the Supporting Information). Measurements at different points on the films have also showed little or no variation in the bistability (Figure S12b in the Supporting Information).

Bistability in the two-dimensional array of dye-coated semiconducting nanoparticles is itself of interest. It shows that a state can be stored in a single hybrid nanoparticle for high-density memory applications. We have characterized a monolayer of the dye and also of the CdS nanoparticles (panels b and c in Figure 7, respectively). Both the monolayers did not yield any bistability in the voltage range (they needed a much higher voltage amplitude to evidence conductance switching). The results hence highlight the advantages of using core−shell hybrid nanoparticles for memory applications. Use of hybrid nanoparticles also allows selecting the core and the shell separately so that a suitable combination can be chosen to match a particular need.

Monolayer of the core−shell nanoparticles, when probed also with a mercury electrode, showed electrical bistability (Figure S13 in the Supporting Information). Here, the on/off ratio is higher than 400; the ratio must hence depend on the work function of the electrode materials. Though a larger area is characterized in the mercury probe method, the results show that bistability is not limited to a doped Si and Pt/Ir electrode combination only. With the mercury electrode, we could also study memory phenomenon in a monolayer of CdS:PB hybrid core−shell nanoparticles. Current under a small probe voltage has depended on the preceding voltage pulse (Figure S14 in the Supporting Information). It is worthwhile to compare the nature of electrical bistability of the core−shell nanoparticles in sandwiched structures and in a monolayer. In the former case, CdS:PB in a PMMA matrix is sandwiched between indium tin oxide (ITO) and Al electrodes having work functions of 4.7 and 4.3 eV, respectively. The devices have yielded a conductance switching to a high state at a suitable negative voltage. Similar results were obtained with fluorine tin oxide (FTO, 4.4−4.6 eV) as

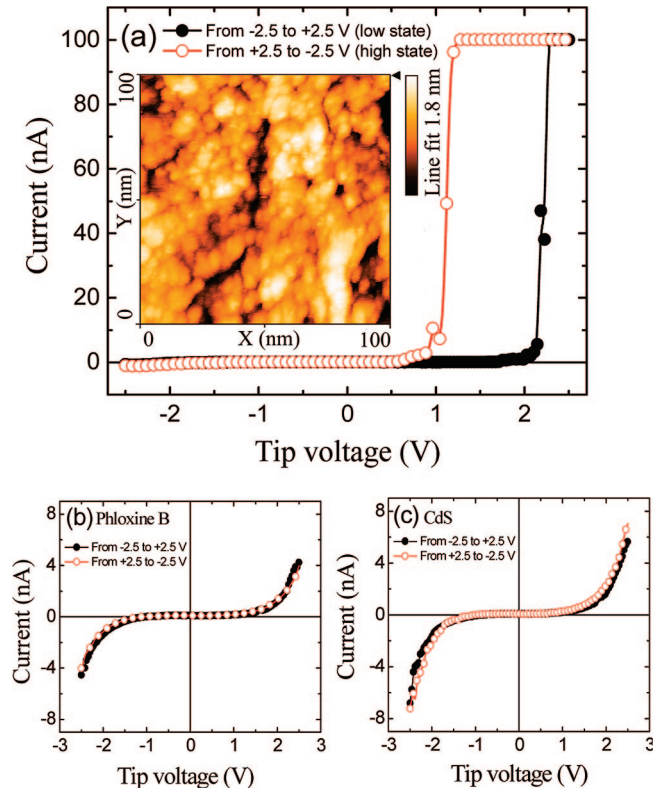

Figure 7. Current−voltage characteristics of a monolayer of (a) CdS:phloxine B hybrid core−shell nanoparticles, (b) phloxine B, and (c) CdS nanoparticles with a STM tip in two sweep directions. Inset of (a) shows a two-dimensional STM topography of a monolayer of CdS:phloxine B hybrid core−shell nanoparticles.

the base electrode. In the monolayer case, the electrode combinations were doped Si (4.9 eV) and Pt/Ir (5.6 eV) or ITO (4.7 eV) and Hg (5.1 eV). Here, switching to a high state occurred at a positive voltage. Since voltage was always applied with respect to the base electrode (ITO or doped Si), the results hence show that the conductance switching occurs when a suitable negative voltage is applied to the low work function electrode. The barrier heights that the charge carriers face must hence have a major role in the observed conductance switching.

To shed light on the mechanism of bistability of core−shell nanoparticles, we have calculated density of states (DOS) before and after conductance switching. Figure 8a shows a plot of d*I*/d*V versus* voltage for the two sweep voltage directions (representing the two conducting states), as obtained from the *I*−*V* characteristics of a monolayer of CdS:PB core−shell with STM as the top electrode. The plot shows that, with an increase in conductance, the total DOS, as calculated from the area under the d*I*/d*V versus* voltage plots, increased with conductance switching. For the monolayer of CdS nanoparticles and PB dye, there was only a little increase in the density of states from a sweep direction to the other (panels b and c in Figure 8, respectively) as compared to that in the hybrid system. This points toward charge confinement in hybrid nanoparticles

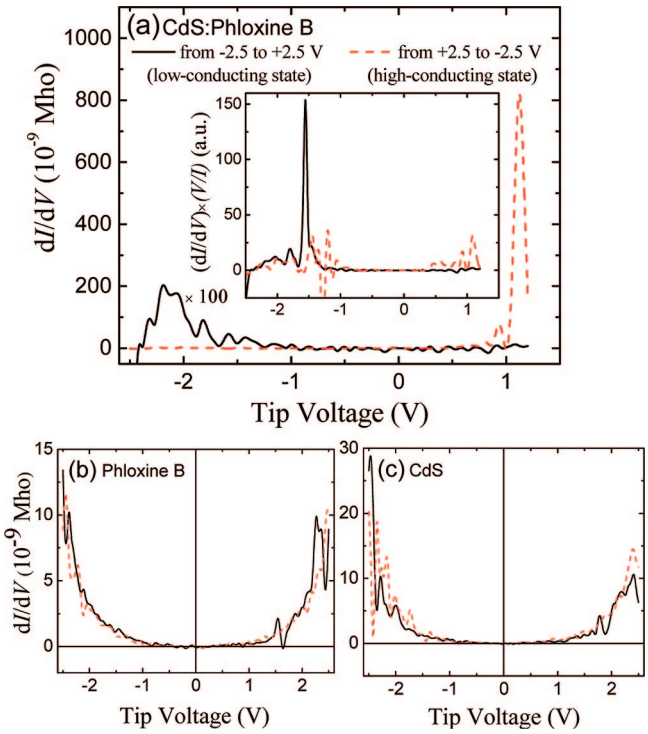

Figure 8. Differential conductance *versus* voltage plots for (a) core−shell hybrid nanoparticles, (b) phloxine B, and (c) CdS nanoparticles. Inset of (a) shows normalized DOS for the core−shell hybrid nanoparticles.

upon conductance switching; the degree of charge confinement was much higher in the core−shell case as compared to the dye or the CdS nanoparticles resulting in higher degree of bistability in dye-coated CdS nanoparticles. The NDOS *versus* voltage plot for the two conducting states are shown in the inset of Figure 8a. The plot shows that, due to conductance switching, available states appeared in the gap—at energies higher than the valence band and lower than the conduction band.

CONCLUSIONS

In conclusion, we have grown core−shell hybrid nanoparticles, formed a monolayer of them, and studied the electrical bistability and memory phenomena. A molecular layer of different anionic dye molecules in the xanthene class was formed on CdS or CdSe quantum dots *via* electrostatic adsorption. The quantum dots were functionalized with cysteamine hydrochloride to enable such an adsorption. We have formed a monolayer of the hybrid nanoparticles on quartz and doped silicon wafers. The monolayer or devices based on the hybrid nanoparticles in an inert polymer matrix have exhibited electrical bistability. Ratio between the conductivities of the two conducting states is several orders higher in magnitude, and threshold voltage of switching is lower in magnitude than the respective values in systems based on the components of the core−shell. Both the factors are advantageous to the addressability of a memory device. The bistability has been due to charge confinement in the nanoparticles. We have shown that electrical bistability and memory phenomena can be achieved in a single organic/inorganic hybrid nanoparticle. This complete study shows the ability to design nanodevices and their memory applications.

METHODS

Materials. Cadmium chloride ($CdCl_2$), sodium sulfite (Na_2SO_3), selenium powder, and sodium sulfide (Na_2S), compounds required to grow CdS and CdSe nanoparticles, were purchased from E-Merck (India). Cysteamine hydrochloride (CAH, M_W = 113.61), purchased from Aldrich Chemicals, was used as a stabilizer for the nanoparticles. Different organic dye molecules in the xanthene class, such as phloxine B (PB), Rose Bengal (RB), erythrosin B (EB), eosin Y (EY), and fluorescein sodium (FS), were also purchased from Aldrich Chemicals. Poly(methyl methacrylate) (PMMA, M_W = 70 000), a matrix material for thin-film formation, was purchased from Aldrich Chemicals. Poly(acrylic acid, sodium salt) (PAA, M_W = 90 000), purchased from Polyscience as a 25% aqueous solution, was the polyanion for monolayer formation and deposition of LbL films *via* electrostatic self-assembly. Deionized water, obtained from Milli-Q Academic System, had a resistivity of 18.2 MΩ · cm. ITO-coated glass substrates for thin-film deposition were purchased from Optical Filters Inc. Strips of ITO were formed by etching with Zn powder and HCl. Polished Si(111) wafers (arsenic doped, N-type) having a resistivity of 3−10 MΩ · cm were purchased from the Institute of Electronic Materials Technology, Poland.

Growth of Quantum Dots. CdS and CdSe nanoparticles were grown following standard reaction route.[10,38,39] While cadmium chloride was used as the source of cadmium ions, Na_2S and Na_2SeSO_3 were the source of sulfur and selenium, respectively. CAH was used as the stabilizer to control the growth of the nanoparticles. To grow CdS quantum dots, typically aqueous solutions of $CdCl_2$ (40 mM, 40 mL), CAH (40 mM, 20 mL), and Na_2S (40 mM, 20 mL) were prepared following vigorous stirring. $CdCl_2$ and the stabilizing agent were first mixed thoroughly; Na_2S solution was then added slowly. The solution turned greenish yellow, evidencing beginning of nucleation. For the growth of CdSe nanoparticles, 1 mL of Na_2SeSO_3 solution, freshly prepared from refluxing (for 10 h) 4.83 g of Na_2SO_3 and 2 g of selenium powder in 100 mL of water, was diluted and added to the mixed solution. After continuous stirring for 6 h and sonication for 30 min, the solution was repeatedly centrifuged at 14 000 rpm (at 5 °C) to separate out the nanoparticles from the dispersed solution. They were finally dried in vacuum at 60 °C.

Formation of Hybrid Core−Shell Nanoparticles. The amine-terminated nanoparticles were first dispersed in deionized water (0.75 mg/mL) to obtain an optically homogeneous solution. The xanthene dyes were also dissolved in water separately (0.1 mM). To obtain dye-coated nanoparticles, equal volumes of both the solutions were added and stirred continuously. Here, the anionic dye molecules become electrostatically bound to the surface of the nanoparticles (at the amine groups) forming hybrid core−shell nanoparticles. The resultant solution was cooled at 5 °C and centrifuged repeatedly at 8000 rpm to separate out the organic−inorganic hybrid nanoparticles. This process was continued until the solvent did not show any trace of the dye. A low speed used during the centrifuge process, moreover, assured that dissolved dye molecules would not become extracted with the hybrid nanoparticles. The products were again dried in vacuum at 60 °C.

Characterization of Nanoparticles. Growth of the nanoparticles was verified following usual characterization methods. Elec-

tronic absorption spectra of the semiconducting quantum dots and organic−inorganic hybrid core−shell nanoparticles in dispersed aqueous solution were recorded with a Shimadzu UV−vis spectrophotometer UV-2550. TEM images and SAED patterns of the particles were recorded through JEOL-JEM 2010. Crystalline phase of the inorganic core was studied by XRD (Rich-Seifert XRD 3000P), SAED patterns, and HR-TEM images. Size of the nanoparticles was also estimated from electronic absorption and the HR-TEM images. Composition of the nanoparticles was examined by EDX analysis. FT-IR spectra of organic−inorganic core−shell nanoparticles, in the form of KBr pellets, were recorded with a Nicolet MAGNA-IR 750 spectrometer.

Monolayer Formation. Organic−inorganic hybrid core−shell nanoparticles were adsorbed electrostatically on protonated polished Si(111) wafers and ITO-coated glass substrates. The substrates were first dipped in a PAA bath for 15 min followed by rinsing thrice in deionized water. To obtain a layer of the nanoparticles, the PAA-coated substrates were dipped in redispersed solution of CdS:dye core−shells followed by the same rinsing protocol. Electrostatic adsorption of the nanoparticles led to the formation of a monolayer or a two-dimensional array of CdS:dye hybrid nanoparticles. To record electronic absorption spectra, films were deposited on quartz substrates. Multilayers of CdS:dye core−shell, to record electronic absorption spectra, were obtained by repeating the PAA and CdS:dye deposition processes in sequence. The films were finally annealed in vacuum at 100 °C.

Electrical Characteristics. The hybrid core−shell nanoparticles, both as thin films in polymer matrices and as a monolayer, were characterized. The core−shell nanoparticles in a PMMA matrix (11.1 wt %) were spun from chloroform solution (2 mg/ml) at a speed of 700 and 1000 rpm, resulting in films of thickness 240−250 and 80−100 nm, respectively. Stripped ITO-coated glass was the substrate for these devices. Individual components, such as CdS or CdSe nanoparticles and the dyes, were also spun individually. Their weight percent in PMMA matrix was kept the same. The thin films were annealed at 100 °C in vacuum. Aluminum, which acted as the other electrode, was thermally evaporated at a pressure below 10^{-5} Torr on top of the films as strips orthogonal to ITO. Thickness of the Al electrode, as obtained from AFM topography of a scratched film, was 100−110 nm. Active area of each of the devices, as determined by the overlap of the electrodes, was 6 mm^2. Current−voltage ($I-V$) characteristics of the devices were recorded with a Yokogawa 7651 dc source, a Keithley 486 picoammeter, and a Keithley 6517A electrometer. Impedance measurements were carried out with a Solartron 1260 Impedance Analyzer with a test ac voltage of 100 mV rms in the 1−12 MHz region.

Monolayer of core−shell nanoparticles and their individual components (CdS, CdSe, and the dyes) were characterized with the mercury probe method and a STM (Nanosurf easyScan 2, Switzerland). While measurements with the mercury drop (on the tip of a metal syringe) were carried out in vacuum, STM measurements were performed in ambient conditions in a constant current mode. A Pt/Ir tip was first approached until a current of 0.5 nA was achieved at 1.5 V. AFM (Nanosurf easyScan 2, Switzerland) images of LbL films, scratched to obtain its depth profile, were recorded to evidence formation of a monolayer.

Acknowledgment. B.C.D. acknowledges CSIR-NET Fellowship No. 09/080(0504)/2006-EMR-I, Roll No. 503982. The authors acknowledge financial support through projects SR/S2/RFCMP-02/2005 and 2007/37/2/BRNS.

Supporting Information Available: Electronic absorption spectra of different hybrid organic−inorganic nanoparticle solutions, electronic absorption spectra of PB at different concentrations, EDX analyses of CdS before and after dye adsorption, XRD spectra of CdS nanoparticles, SAED pattern of CdS and CdSe before and after dye adsorption, FT-IR spectra of CdS with and without PB adsorption, $I-V$ characteristics ITO/CdS:PB/Al devices with different V_{max} values and under multiple voltage loops, rectifying the nature of $I-V$ characteristics, ln(I) *versus* $V^{1/2}$ and ln(G) *versus* $E^{-1/2}$ plots for the low and high conducting states, respectively, Cole−Cole plot, STM topographies of a section of a monolayer, $I-V$ characteristics of a CdS:PB monolayer with different V_{max} values and at different points on the monolayer, $I-V$ characteristics, and OM application of a monolayer of CdS:PB with mercury as the other electrode. This material is available free of charge *via* the Internet at http://pubs.acs.org.

REFERENCES AND NOTES

1. Murray, C. B.; Norris, D. J.; Bawendi, M. G. Synthesis and Characterization of Nearly Monodisperse CdE (E = S, Se, Te) Semiconductor Nanocrystallites. *J. Am. Chem. Soc.* **1993**, *115*, 8706–8715.
2. Wang, Y. A.; Li, J. J.; Chen, H. Y.; Peng, X. G. Stabilization of Inorganic Nanocrystals by Organic Dendrons. *J. Am. Chem. Soc.* **2002**, *124*, 2293–2298.
3. Paul, S.; Pearson, C.; Molloy, A.; Cousins, M. A.; Green, M.; Kolliopoulou, S.; Dimitrakis, P.; Normand, P.; Tsoukalas, D.; Petty, M. C. Langmuir−Blodgett Film Deposition of Metallic Nanoparticles and Their Application to Electronic Memory Structures. *Nano Lett.* **2003**, *3*, 533–536.
4. Lee, D.; Rubner, M. F.; Cohen, R. E. All-Nanoparticle Thin-Film Coatings. *Nano Lett.* **2006**, *6*, 2305–2312.
5. Kotov, N. A.; Dekany, I.; Fendler, J. H. Layer-by-Layer Self-Assembly of Polyelectrolyte-Semiconductor Nanoparticle Composite Films. *J. Phys. Chem.* **1995**, *99*, 13065–13069.
6. Ariga, K.; Hill, J. P.; Ji, Q. M. Layer-by-Layer Assembly as a Versatile Bottom-up Nanofabrication Technique for Exploratory Research and Realistic Application. *Phys. Chem. Chem. Phys.* **2007**, *9*, 2319–2340.
7. Vittal, J. J.; Ng, M. T. Chemistry of Metal Thio- and Selenocarboxylates: Precursors for Metal Sulfide/Selenide Materials, Thin Films, and Nanocrystals. *Acc. Chem. Res.* **2006**, *39*, 869–877.
8. Colvin, V. L.; Schlamp, M. C.; Alivisatos, A. P. Light-Emitting-Diodes Made from Cadmium Selenide Nanocrystals and a Semiconducting Polymer. *Nature* **1994**, *370*, 354–357.
9. Zhang, Q.; Atay, T.; Tischler, J. R.; Bradley, M. S.; Bulovic, V.; Nurmikko, A. V. Highly Efficient Resonant Coupling of Optical Excitations in Hybrid Organic/Inorganic Semiconductor Nanostructures. *Nat. Nanotechnol.* **2007**, *2*, 555–559.
10. Das, B. C.; Pal, A. J. Memory Applications and Electrical Bistability of Semiconducting Nanoparticles: Do the Phenomena Depend on Bandgap. *Small* **2008**, *4*, 542.
11. Portney, N. G.; Martinez-Morales, A. A.; Ozkan, M. Nanoscale Memory Characterization of Virus-Templated Semiconducting Quantum Dots. *ACS Nano* **2008**, *2*, 191–196.
12. Peng, X. G.; Schlamp, M. C.; Kadavanich, A. V.; Alivisatos, A. P. Epitaxial Growth of Highly Luminescent Cdse/Cds Core/Shell Nanocrystals with Photostability and Electronic Accessibility. *J. Am. Chem. Soc.* **1997**, *119*, 7019–7029.
13. Caruso, F. Nanoengineering of Particle Surfaces. *Adv. Mater.* **2001**, *13*, 11–22.
14. Reiss, P.; Bleuse, J.; Pron, A. Highly Luminescent CdSe/ZnSe Core/Shell Nanocrystals of Low Size Dispersion. *Nano Lett.* **2002**, *2*, 781–784.
15. Zhou, H. S.; Sasahara, H.; Honma, I.; Komiyama, H.; Haus, J. W. Coated Semiconductor Nanoparticles—The CdS/PbS System's Photoluminescence Properties. *Chem. Mater.* **1994**, *6*, 1534–1541.
16. Skaff, H.; Sill, K.; Emrick, T. Quantum Dots Tailored with Poly(Para-Phenylene Vinylene). *J. Am. Chem. Soc.* **2004**, *126*, 11322–11325.
17. Chan, W. C. W.; Nie, S. M. Quantum Dot Bioconjugates for Ultrasensitive Nonisotopic Detection. *Science* **1998**, *281*, 2016–2018.
18. Pellegrino, T.; Kudera, S.; Liedl, T.; Javier, A. M.; Manna, L.; Parak, W. J. On the Development of Colloidal Nanoparticles Towards Multifunctional Structures and Their Possible Use for Biological Applications. *Small* **2005**, *1*, 48–63.

19. Klostranec, J. M.; Chan, W. C. W. Quantum Dots in Biological and Biomedical Research: Recent Progress and Present Challenges. *Adv. Mater.* **2006**, *18*, 1953–1964.
20. Sasaki, T.; Ebina, Y.; Tanaka, T.; Harada, M.; Watanabe, M.; Decher, G. Layer-by-Layer Assembly of Titania Nanosheet/Polycation Composite Films. *Chem. Mater.* **2001**, *13*, 4661–4667.
21. Clapp, A. R.; Medintz, I. L.; Mauro, J. M.; Fisher, B. R.; Bawendi, M. G.; Mattoussi, H. Fluorescence Resonance Energy Transfer between Quantum Dot Donors and Dye-Labeled Protein Acceptors. *J. Am. Chem. Soc.* **2004**, *126*, 301–310.
22. Lim, I. I. S.; Goroleski, F.; Mott, D.; Kariuki, N.; Ip, W.; Luo, J.; Zhong, C. J. Adsorption of Cyanine Dyes on Gold Nanoparticles and Formation of J-Aggregates in the Nanoparticle Assembly. *J. Phys. Chem. B* **2006**, *110*, 6673–6682.
23. Mohanta, K.; Majee, S. K.; Batabyal, S. K.; Pal, A. J. Electrical Bistability in Electrostatic Assemblies of CdSe Nanoparticles. *J. Phys. Chem. B* **2006**, *110*, 18231–18235.
24. Verbakel, F.; Meskers, S. C. J.; Janssen, R. A. J. Electronic Memory Effects in Diodes from a Zinc Oxide Nanoparticle-Polystyrene Hybrid Material. *Appl. Phys. Lett.* **2006**, *89*, 102103.
25. Jung, J. H.; Kim, J. H.; Kim, T. W.; Song, M. S.; Kim, Y. H.; Jin, S. Nonvolatile Organic Bistable Devices Fabricated Utilizing Cu_2O Nanocrystals Embedded in a Polyimide Layer. *Appl. Phys. Lett.* **2006**, *89*, 122110.
26. Das, B. C.; Batabyal, S. K.; Pal, A. J. A Bit Per Particle: Electrostatic Assembly of Cdse Quantum Dots as Memory Elements. *Adv. Mater.* **2007**, *19*, 4172–4176.
27. Verbakel, F.; Meskers, S. C. J.; Janssen, R. A. J. Surface Modification of Zinc Oxide Nanoparticles Influences the Electronic Memory Effects in ZnO-Polystyrene Diodes. *J. Phys. Chem. C* **2007**, *111*, 10150–10153.
28. Li, F. S.; Son, D. I.; Cha, H. M.; Seo, S. M.; Kim, B. J.; Kim, H. J.; Jung, J. H.; Kim, T. W. Memory Effect of CdSe/ZnS Nanoparticles Embedded in a Conducting Poly[2-Methoxy-5-(2-Ethylhexyloxy)-1,4-Phenylene-Vinylene] Polymer Layer. *Appl. Phys. Lett.* **2007**, *90*, 222109.
29. Bandhopadhyay, A.; Pal, A. J. Large Conductance Switching and Binary Operation in Organic Devices: Role of Functional Groups. *J. Phys. Chem. B* **2003**, *107*, 2531–2536.
30. Ma, D.; Aguiar, M.; Freire, J. A.; Hummelgen, I. A. Organic Reversible Switching Devices for Memory Applications. *Adv. Mater.* **2000**, *12*, 1063–1066.
31. Yang, Y.; Ma, L. P.; Wu, J. H. Organic Thin-Film Memory. *MRS Bull.* **2004**, *29*, 833–837.
32. Donhauser, Z. J.; Mantooth, B. A.; Kelly, K. F.; Bumm, L. A.; Monnell, J. D.; Stapleton, J. J.; Price, D. W.; Rawlett, A. M.; Allara, D. L.; Tour, J. M.; et al. Conductance Switching in Single Molecules through Conformational Changes. *Science* **2001**, *292*, 2303–2307.
33. Collier, C. P.; Wong, E. W.; Belohradsky, M.; Raymo, F. M.; Stoddart, J. F.; Kuekes, P. J.; Williams, R. S.; Heath, J. R. Electronically Configurable Molecular-Based Logic Gates. *Science* **1999**, *285*, 391–394.
34. Solak, A. O.; Ranganathan, S.; Itoh, T.; McCreery, R. L. A Mechanism for Conductance Switching in Carbon-Based Molecular Electronic Junctions. *Electrochem. Solid State Lett.* **2002**, *5*, E43–E46.
35. Ssenyange, S.; Yan, H. J.; McCreery, R. L. Redox-Driven Conductance Switching *via* Filament Formation and Dissolution in Carbon/Molecule/TiO_2/Ag Molecular Electronic Junctions. *Langmuir* **2006**, *22*, 10689–10696.
36. Yu, D.; Wang, C. J.; Wehrenberg, B. L.; Guyot-Sionnest, P. Variable Range Hopping Conduction in Semiconductor Nanocrystal Solids. *Phys. Rev. Lett.* **2004**, *92*, 216802.
37. Macdonald, J. R. Theory of Ac Space-Charge Polarization Effects in Photoconductors, Semiconductors, and Electrolytes. *Phys. Rev.* **1953**, *92*, 4–17.
38. Colvin, V. L.; Goldstein, A. N.; Alivisatos, A. P. Semiconductor Nanocrystals Covalently Bound to Metal-Surfaces with Self-Assembled Monolayers. *J. Am. Chem. Soc.* **1992**, *114*, 5221–5230.
39. Rao, C. N. R.; Vivekchand, S. R. C.; Biswas, K.; Govindaraj, A. Synthesis of Inorganic Nanomaterials. *Dalton Trans.* **2007**, 3728–3749.